Supporting Information

Modified adsorption energies on single-layer IrO_2 and RuO_2 films of IrO_2-RuO_2 heterostructures: Localized effect of subsurface metal-oxygen ligands

Suriya Ramasubramanian[1], Jisu Shin[1], Christopher J. Lee[1], Chethana Sudarshan[1], Omar Almarshad[1], Alvaro Loaiza Orduz[3], Randall J. Meyer[2], Craig Plaisance,[3,*] David Hibbitts[1,4*] and Jason F. Weaver[1,*]

[1]Department of Chemical Engineering, University of Florida, Gainesville, FL 32611, USA

[2]ExxonMobil Research and Engineering, Annandale, NJ 08801, USA

[3]Cain Department of Chemical Engineering, Louisiana State University, Baton Rouge, LA 70803, USA

[4]Davidson School of Chemical Engineering, Purdue University, West Lafayette, IL 47907, USA

*To whom correspondence should be addressed, weaver@che.ufl.edu, hibbitts@purdue.edu, plaisance@lsu.edu

S1. Experimental Details

The experiments reported in this study were conducted in an ultrahigh vacuum (UHV) chamber with a typical base pressure of 3×10^{-10} Torr.[1-4] The UHV chamber is equipped with a four-grid retarding field analyzer for low energy electron diffraction (LEED) and Auger electron spectroscopy (AES), an ion sputter gun, a quadrupole mass spectrometer (QMS) used for TPD experiments and two electron-beam metal evaporators (McAllister Technical Services) for the vapor deposition of iridium and ruthenium, respectively. A single-stage differentially pumped chamber attached to the main UHV chamber houses an inductively coupled RF plasma source that is used to generate atomic oxygen beams.

The Ru(0001) single crystal (9 mm × 1 mm) used in this study was attached to 0.40 mm tungsten wires mounted on an LN_2 cooled sample holder. A type K thermocouple was spot welded onto the back side of the sample for temperature measurements. Resistive heating, controlled using a PID controller that varies the output of a programmable DC power supply, supports linear ramping from 85 to 1450 K and maintaining a desired temperature. The sample was cleaned by several cycles of Ar^+ sputtering (2 keV) at 900 K followed by annealing at 1400 K until no impurities were detected by AES and a sharp LEED pattern was obtained.

We investigated the binding properties of the oxide surfaces using N_2 and O_2 (Airgas, 99.999%) TPD experiments. In these experiments, the sample was exposed to N_2 and O_2 at 94 K and 300 K, respectively, in quantities that saturated the N_2 and O_t adlayers. After exposure, the sample was positioned in front of a shielded mass spectrometer at a distance of ~5 mm and heated at a constant rate of 1 K/s. After each TPD experiment, the sample was exposed to 10 L of O_2 at 300 K and subsequently heated to 600 K to restore oxygen vacancies that may have been created during the TPD experiment.[5-8] Reproducibility in our TPD results provides evidence that $IrO_2(110)$ and $RuO_2(110)$ films with nominally the same surface structure and composition can be repeatedly generated.

Film growth procedure

Layered IrO_2/RuO_2 heterostructures were prepared using a stepwise approach wherein $IrO_2(110)$ was first grown in varying coverages on $RuO_2(110)$ and characterized,[9-11] and $RuO_2(110)$ was then

grown in small steps on a thick $IrO_2(110)$ film. Close lattice matching allows $IrO_2(110)$ to grow epitaxially on the $RuO_2(110)$ surface and vice versa; an $IrO_2(110)$ layer on $RuO_2(110)$ is estimated to experience strain of only +1.6% and -0.3% along the [001] and [$\bar{1}$10] directions, respectively.[9-12] In the first step of the growth, a s-$RuO_2(110)$ thin film of about 4.2 nm thickness was generated by exposing clean Ru(0001) to an O-atom beam at 750 K, where the film thickness of 4.2 nm is equivalent to about 13 "layers" of $RuO_2(110)$ as defined in the main text.[13-17]

Two approaches were used to grow $IrO_2(110)$ on the $RuO_2(110)$ substrate. For low IrO_2 coverages (< 0.9 layers), metallic Ir were deposited in small coverages from an e-beam evaporator at a sample temperature of 300 K and subsequently oxidized by exposure to an O-atom beam with the sample held at 700 K. This approach was used to increase the $IrO_2(110)$ coverage in steps of only ~0.2 layers, and enable characterization of the development and binding properties of 1L-$IrO_2(110)$ domains at several coverages. After depositing a total of 0.9 layers, the $IrO_2(110)$ coverage was increased in larger steps (0.5 to 3 layers) by depositing Ir in an O_2 background of 8×10^{-7} Torr at a surface temperature of 700 K, followed by post-oxidation using an O-atom beam. The final $IrO_2(110)$ film that was studied had a thickness of 5.4 layers, and exhibits chemical properties that are characteristic of bulk-like $IrO_2(110)$ as shown previously.[8-9] After each IrO_2 growth step, the surface was exposed to 10 L (Langmuir) of O_2 at 600 K to further clean the surface and fill bridging oxygen (O_{br}) vacancies that may have formed, and then characterized using TPD to probe the binding of N_2 and O_t. The O_2 cleaning procedure was also applied after each TPD experiment. The TPD spectra were highly reproducible for each IrO_2 coverage, demonstrating that the $IrO_2/RuO_2(110)$ structures changed negligibly during the N_2 and O_t TPD experiments as well as during exposure to O_2 at 600 K.

After completing experiments with IrO_2 on $RuO_2(110)$, RuO_2 was grown in steps on the 5.4-layer $IrO_2(110)$ film using the procedures discussed above. For low RuO_2 coverages (< 1.1 layers), RuO_2 was grown on $IrO_2(110)$ by depositing small coverages of metallic Ru from an e-beam evaporator at a sample temperature of 300 K and then oxidizing by exposure to an O-atom beam at 700 K. This post-oxidation approach was used to increase the RuO_2 coverage to about 1.1 layers in steps of ~0.2 layers, and thereafter the $RuO_2(110)$ coverage was increased in larger steps by depositing Ru in an O_2 background of 8×10^{-7} Torr, until reaching a $RuO_2(110)$ thickness of about 3.3 layers. LEED confirms that the IrO_2/RuO_2 layered heterostructures maintain the (110)

orientation of the initial $RuO_2(110)$ growth substrate (Figure S1), and both AES and XPS demonstrate that the IrO_2 and RuO_2 layers mix negligibly in the experiments, when the temperature is maintained below 700 K.[13]

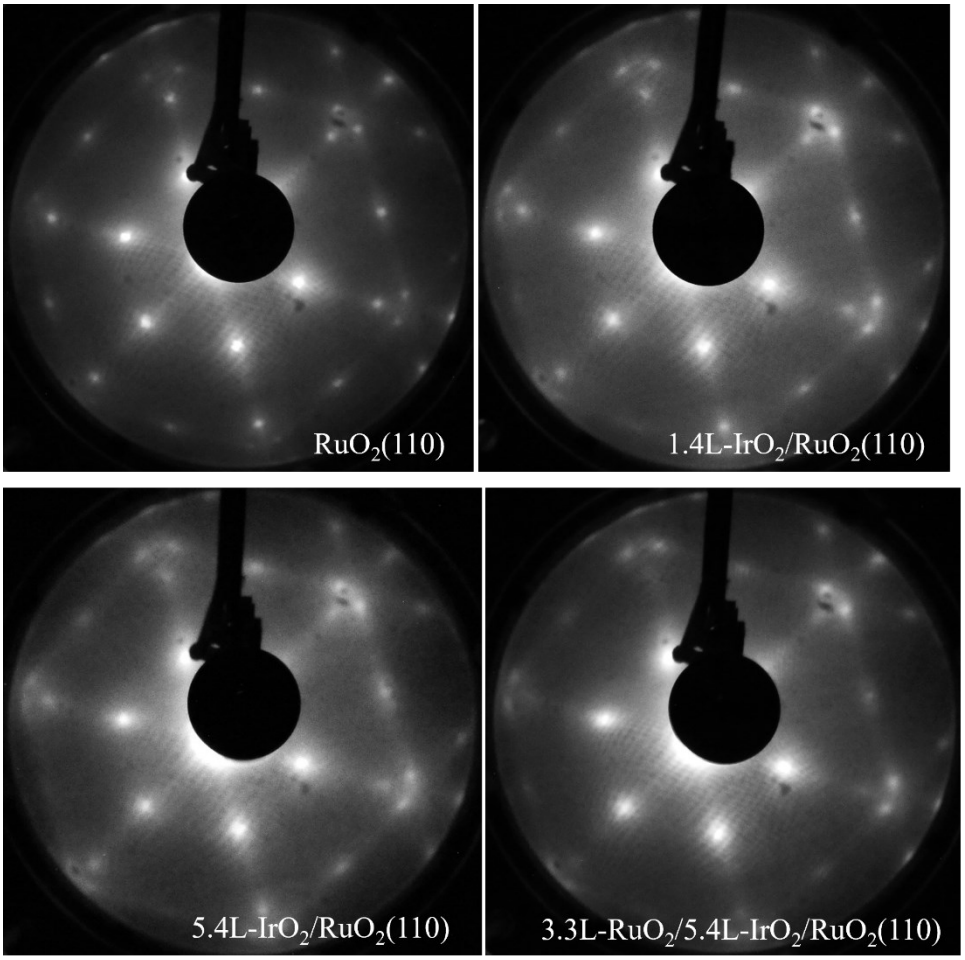

Figure S1. Representative LEED images acquired from the initial ~13-layer $RuO_2(110)$ film grown on Ru(0001) and 1.4L-$IrO_2/RuO_2(110)$, 5.4L-$IrO_2/RuO_2(110)$ and 3.3L-RuO_2/5.4L-$IrO_2/RuO_2(110)$ film structures. The initial $RuO_2(110)$ film grows in three rotationally degenerate domains on Ru(0001), giving rise to the characteristic triplets observed in the LEED pattern.[9, 18] The (110) LEED pattern is maintained for IrO_2 films grown on $RuO_2(110)$ and RuO_2 films grown on $IrO_2/RuO_2(110)$, confirming epitaxial growth of these heterostructures. Broadening of the LEED spots suggests that the layered films are less crystalline than the initial $RuO_2(110)$ surface, likely indicating that the deposits form smaller domains than the initial film.

S2. Estimating the IrO_2 and RuO_2 coverages

The coverages of IrO_2 and RuO_2 grown on RuO_2(110) and IrO_2(110), respectively, were computed using estimates of the Ir or Ru fluences (flux*exposure time), determined after calibrating the Ir and Ru fluxes generated by the e-beam evaporators. The Ir flux was estimated by depositing metallic Ir onto Ru(0001) for varying times, and relating the attenuation of the Ru MNN AES peak at 274 eV to the Ir coverage. The decrease in the Ru AES peak intensity was related to the thickness (z) of the Ir overlayer from the equation, $I = I_o \exp(-z/\lambda_{Ir})$ where I_o is the peak intensity for clean Ru(0001) and λ_{Ir} is the inelastic mean free path (IMFP) of the Ru Auger electrons (KE = 274 eV) through metallic Ir. The IMFP used in the calculations (λ_{Ir} = 6.07 Å) was determined from the TPP equation.[19] The thickness of the Ir overlayer was converted to a coverage by assuming that a full monolayer of metallic Ir on Ru(0001) (1 Ir atom per Ru(0001) unit cell) has a height (2.2 Å) equal to the spacing between Ir(111) planes. For IrO_2(110) the repeating structure along the [110] direction has an Ir density that is 70% of that of the close-packed Ir(111) planes. This difference in Ir density was used to estimate the IrO_2 coverages generated in the experiments by converting the Ir fluence to units of IrO_2 layers, as defined in the main text. After depositing a thick Ir layer on Ru(0001), Ru was deposited on the surface for varying times and its flux was estimated by monitoring the intensification of the Ru MNN peak, and describing the peak intensity using the formula,[20]

$$I = I_o \exp\left(-\frac{z}{\lambda_{Ru}}\right) + I_\infty \left(1 - \exp\left(-\frac{z}{\lambda_{Ru}}\right)\right)$$

where z is the thickness of the Ru layer deposited onto Ir, I_o is the Ru MNN peak intensity from the Ir covered Ru(0001) surface prior to Ru deposition, I_∞ is the Ru MNN peak intensity from clean Ru(0001) and λ_{Ru} is the IMFP for the Ru AES electrons traveling through Ru. A value of λ_{Ru} = 6.24 Å, estimated from the TPP equation, was used in the calculations. In this equation, the term with I_o represents the contribution from the underlying Ru(0001) substrate, and the term with I_∞ represents the contribution from the Ru film grown on the Ir-covered Ru(0001) surface.[20] Figure S2 shows the calibration curves generated in these experiments.

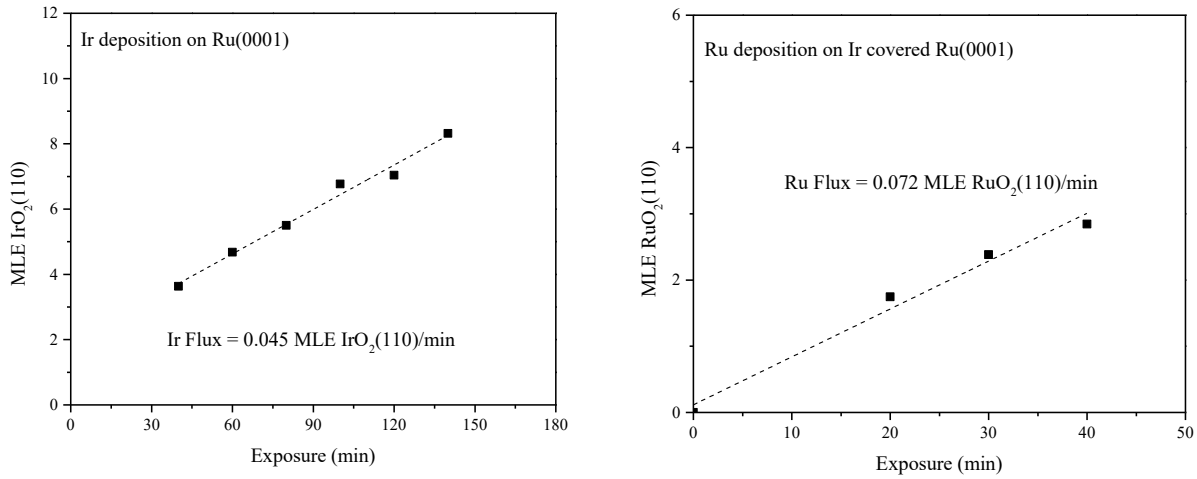

Figure S2. Thicknesses of an Ir layer grown on Ru(0001) (left) and a Ru layer grown on Ir-covered Ru(0001) (right) as a function of exposure time (min) to Ir or Ru vapor, respectively, supplied by e-beam evaporators. The overlayer thicknesses are given in units of MLE (monolayer equivalent) of $IrO_2(110)$ or $RuO_2(110)$, as described in the text. From the slopes of these curves, we estimate the metal fluxes used in our experiments as Ir flux = 0.045 ± 0.003 MLE $IrO_2(110)$/min and Ru flux = 0.072 ± 0.007 MLE $RuO_2(110)$/min where the uncertainties are given by the standard errors of the linear regressions.

S3. TPD analysis to estimate N_2 and O_t binding energies

The binding energies of N_2 and O_t were estimated from the experimental TPD data using the Redhead equation.[21] Desorption pre-factors were determined using a previously reported 3*N* model in which all adsorbate motions are treated as harmonic oscillations and all vibrational partition functions are set equal to one.[22] The 3*N* model provides an approximate upper bound for the desorption pre-factors, and implies that species adsorbed on M_{cus} sites are effectively immobile due to large in-plane corrugation in the potential energy surface. We have previously reported that the 3*N* model provides accurate pre-factors for the desorption of several species from $IrO_2(110)$ and $RuO_2(110)$, including alkanes, N_2, H_2 and O_2.[6-7, 9, 17, 23-25] The transition state theory formula for a desorption pre-factor (A_{des}) is given in terms of molecular partition functions by the expression,

$$A_{des} = \frac{kT}{h}\frac{(q_t q_r q_v)_{2Dgas}}{q_{v,ads}}$$

where q_t, q_r and q_v represent partition functions for translation, rotation and vibration of the adsorbate or the 2D-gas transition state. For the 3*N* model, the vibrational partition functions are set equal to one and the pre-factor equation simplifies to the following,

$$A_{des} = \frac{kT}{h}\frac{2\pi mkT}{h^2}A\frac{8\pi^2 IkT}{h^2}$$

where m and I represent the mass and moment of inertia of the desorbing molecule, and A represents the area occupied by the adsorbate, which is set equal to that of the $MO_2(110)$ surface unit cell, i.e., $A = 2 \times 10^{-19}$ m^2.[18, 26] The value of A used for all surfaces was determined from the dimensions of the $IrO_2(110)$ surface unit cell, neglecting the small differences in lattice constant of RuO_2 and IrO_2. Finally, the 3*N* model gives an equation for the desorption pre-factors of diatomic molecules of the form, $A_{des} = CT^3$ where C is a species and surface dependent constant with values of 6.6×10^9 and 1.0×10^{10} s^{-1} K^{-3}, for N_2 and O_2, respectively, for the $IrO_2(110)$ and $RuO_2(110)$ surfaces. Table S1 lists the TPD peak temperatures, desorption pre-factors and binding energies computed using the Redhead equation for the desorption of N_2 and O_2 from 1L and nL IrO_2 and RuO_2 thin films.

Table S1. TPD peak temperatures, desorption pre-factors from the 3*N* model and the N_2 and O_t adsorption energies determined from Redhead analysis for N_2 and O_2 desorption from 1L and nL RuO_2 and IrO_2 thin films. The N_2 and O_t adsorption energies are obtained from $E_{ads,N2} = -E_{des,N2}$ and $E_{ads,Ot} = -0.5*E_{des,O2}$ where $E_{des,N2}$ and $E_{des,O2}$ are the activation energies for molecular N_2 desorption and recombinative O_t desorption, respectively.

	O_t binding			**N_2 binding**		
Surface	T_p (K)	log(A_{des} (s^{-1}))	E_{ads} (kJ/mol)	T_p (K)	log(A_{des} (s^{-1}))	E_{ads} (kJ/mol)
nL-RuO_2	400	17.8	-73	175	16.5	-59
1L-RuO_2/IrO_2	530	18.2	-100	200	16.7	-68
nL-IrO_2	463	18.0	-86	275	17.1	-96
1L-IrO_2/RuO_2	340	17.6	-62	240	17.0	-83

S4. Computational Details

Periodic, plane-wave DFT computations are carried out using the Vienna ab initio simulation package (VASP).[27-30] as provided in the computational catalysis interface (CCI).[31] The Perdew–Burke–Ernzerhof (PBE),[32] revised PBE (RPBE) exchange–correlation functional,[33] and Bayesian Error Estimation Functional (BEEF) were employed,[34] and plane waves were constituted of projector augmented wave pseudopotentials (PAWs) with an energy cutoff of 400 eV.[35-36] To capture dispersive (i.e., van der Waals) interactions, calculations with and without the D3 methods were also performed.[37-38] Calculations involving $IrO_2(110)$ and $RuO_2(110)$ were run with second-order Methfessel-Paxton smearing with 0.2 eV width, as both oxides are fully conducting. Calculations were performed with and without spin polarization to determine whether the oxide surfaces, with or without adsorbates, had magnetic moments and to accurately capture their binding properties.

Fig. 1. shows ball-and-stick models of 4 × 2 unit cells for (a) $IrO_2(110)$ and (b) $RuO_2(110)$. The models consist of 4-layer slabs and 13 Å vacuum gaps between periodic images. Both surfaces are made of alternating rows of cus-metal atoms (M_{cus}) and rows of bridging O atoms (O_{br}). The $IrO_2(110)$ surface unit cell is rectangular, with bulk-terminated dimensions of a= 3.19 Å and b = 6.42 Å, while for $RuO_2(110)$ they are a = 3.12 Å and b= 6.39 Å. The $IrO_2(110)$ and $RuO_2(110)$ surface models, consisting of 1 × 1, 2 × 1, 3 × 1 and 4 × 1 unit cells, were investigated to reduce computational cost while ensuring reproducibility of binding energies and magnetic moments. The models were optimized by PBE, and a 25 × 25 × 35 Monkhorst-Pack k-point mesh was used for the bulk calculations, with atomic positions optimized until forces were less than 0.01 eV A^{-1}. The Ir_{cus}, Ru_{cus} and O_{br} atoms each have a single dangling bond due to the decrease in bond coordination relative to bulk $IrO_2(110)$ and $RuO_2(110)$; the Ir_{cus} and the Ru_{cus} atoms have five-fold coordination, whereas bulk Ir and Ru atoms have sixfold coordination, and O_{br} atoms have two-fold coordination, whereas bulk O-atoms have three-fold coordination. On-top oxygen atoms (O_t) bond directly on Ir_{cus} or Ru_{cus} atoms and expose a dangling bond perpendicular to the surface. A 3 × 3 × 1 k-point mesh was used for the slab calculations. Structures were optimized in a two-step sequence, with an initial optimization until forces on unconstrained atoms were less than 0.05 eV A^{-1}. Forces in this step were computed using a fast Fourier transform (FFT) grid 1.5× the planewave energy cutoff. In the second step, forces were computed and converged to the same

force criteria, with the bottom two layers fixed and the remaining layers relaxed. A 3 × 3 × 5 sampling of the Brillouin zone was used.

Gas phase O_2 and N_2 were modelled in a 10 × 10 × 10 Å unit cell. Atomic positions were optimized until forces were less than 0.05 eV A^{-1}. Calculations for O_2 were performed spin-polarized to accurately capture its triplet state. On the surfaces, O_t and N_2^* preferentially bind to coordinatively unsaturated metal (M_{cus}) sites, while O_2* binds in a di-σ configuration across a pair of M_{cus}.[18, 26, 39-40] All unique coverages and configurations up to 1 monolayer (ML) were considered for each adsorbate.

The adsorption energy (E_{ads}) is the energy required to adsorb adsorbates (O_t, O_2*, and N_2*) from adsorbate-covered surfaces and a bare surface and is shown here for O_t:

$$E_{ads} = E[\mathrm{O_t}] - 1/2 \cdot E[\mathrm{O_2}] - E[\mathrm{surf}] \quad (1)$$

O_2 dissociation and diffusion on the surfaces were evaluated using the nudged elastic band method (NEB)[41-42] using 12–16 images. In NEB calculations, the pathway was minimized until forces on all unconstrained atoms were less than 0.5 eV A^{-1}, as NEB is only used here to generate a rough guess of the minimum energy pathway. Transition state structures were predicted using the dimer method and the NEB results. The dimer method uses a pair of structures to estimate the potential energy surface's local curvature until it converges on a saddle point.[43] Transition state structures were optimized until the maximum force on unconstrained atoms was less than 0.05 eV A^{-1}, identical to the methods used for optimized O_2*, O_t, and N_2* calculations.

S5. DFT calculations for N_2 and O_t binding energies on mixtures

Figure S3 illustrates the relative energies and configurations of O_2 adsorption, dissociation, and O_t diffusion on (110) surfaces. When O_2(g) approaches the IrO_2 surface, it initially forms superoxo O_2* with a binding energy of −36 kJ mol^{-1}, followed by *O-O* formation with −188 kJ mol^{-1}. The O-O dissociation requires overcoming an energy barrier of 16 kJ mol^{-1} to form two adjacent O_t atoms with a binding energy of −216 kJ mol^{-1}. The barriers for O_t diffusion on IrO_2(110) are substantial, measuring 138 kJ mol^{-1} higher than the 2 O_t close state. For the 2 O_t far state, the barrier is 137 kJ mol^{-1}. Notably, the diffusion process is essentially thermoneutral, with only a 1 kJ mol^{-1} difference between the 2 O_t close and far states. Similar to IrO_2, other surfaces exhibit comparable trends, showing steep energy decreases when forming the 2 O_t close state. The binding energies of the 2 O_t close state are −169, −196, −216, and −248 kJ mol^{-1} for 1L IrO_2/RuO_2, RuO_2, IrO_2, and 1L RuO_2/IrO_2, respectively, aligning with the order of O_t adsorption energies presented in Figure 5.

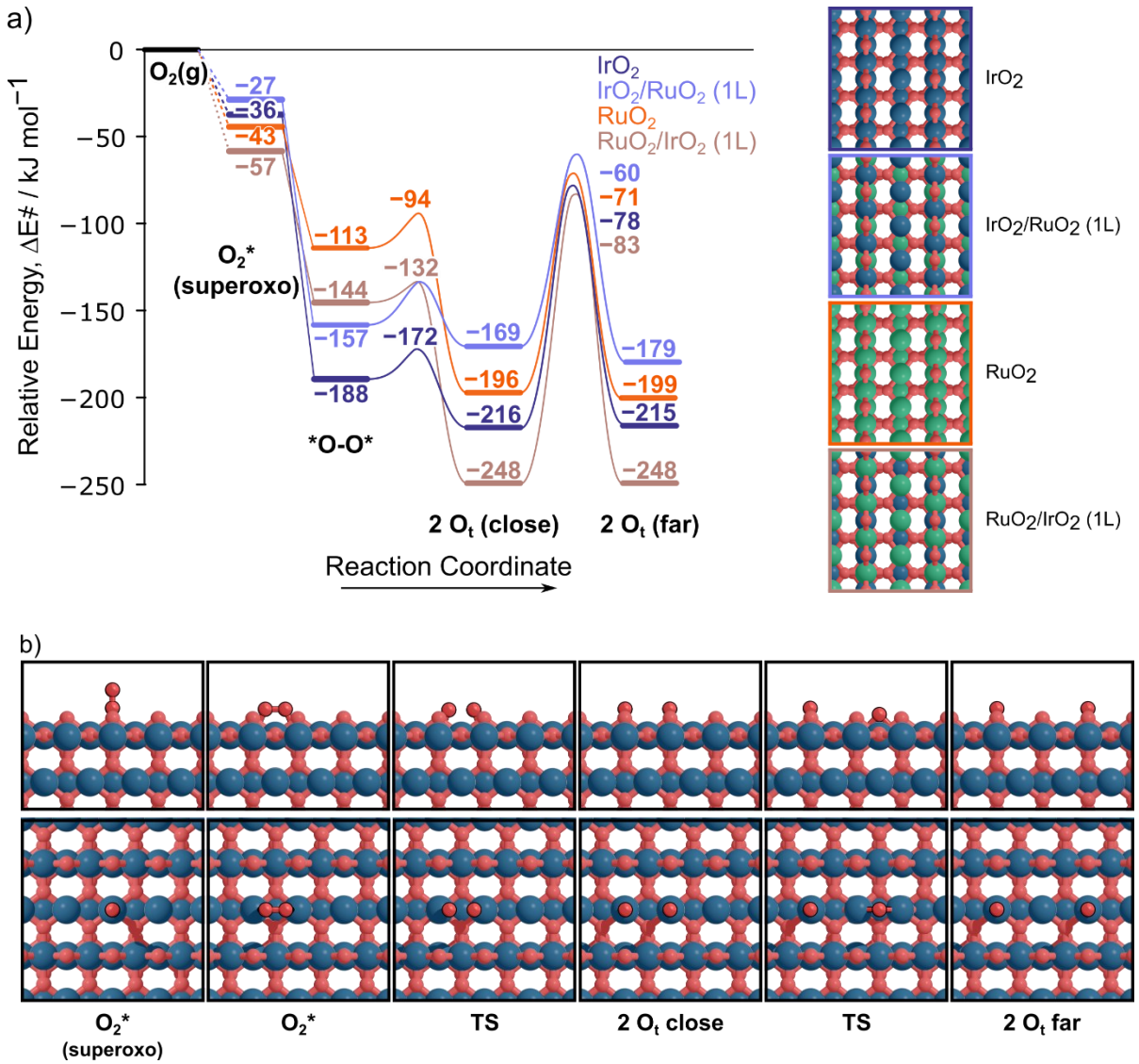

Figure S3. Energy levels of O_2 on (a) IrO_2, IrO_2/RuO_2 (1L), RuO_2, and RuO_2/IrO_2 (1L) surfaces, calculated for various configurations of molecular (O_2(g), O_2*, *O-O*) and atomic (O_t) oxygen, illustrated in (b) the adsorption and diffusion processes. Green atoms represent Ru, dark blue atoms represent Ir, and red atoms represent O.

Table S2 presents adsorption energies of O_t and N_2 on (110) surfaces of pure and layered structures. For O_t binding, the RPBE functional demonstrates the best agreement with TPD results, showing differences of 1, 11, 19, and 10 kJ mol^{-1} on IrO_2, IrO_2/RuO_2, RuO_2, and 1L RuO_2/IrO_2, respectively. However, other methods also exhibit similar trends to the RPBE and TPD results, suggesting that functional choice and spin-polarization applications are not critical factors in calculating O_t adsorption energies. For N_2 binding, the BEEF-spin functional shows optimal agreement with TPD results, with differences of only 7, 1, 1, and 6 kJ mol^{-1} for IrO_2, 1L IrO_2/RuO_2, RuO_2, and 1L RuO_2/IrO_2, respectively. Similar to the O_t results, other functionals and spin-polarization considerations demonstrate comparable trends with N_2 TPD results, indicating robustness across computational approaches.

Table S2. Adsorption energies of O_t and N_2 on the (110) surfaces of IrO_2, 1L-IrO_2/RuO_2, RuO_2, and 1L-RuO_2/IrO_2 calculated using various functionals (PBE, PBE-spin, BEEF, BEEF-spin, RPBE and RPBE-spin). All the values are given in kJ mol^{-1}.

	O_t							N_2						
	TPD	PBE	PBE-spin	BEEF	BEEF-spin	RPBE	RPBE-spin	TPD	PBE	PBE-spin	BEEF	BEEF-spin	RPBE	RPBE-spin
IrO_2	−86	−104	−109	−100	−107	−87	−94	−96	−111	−111	−102	−103	−82	−83
1L-IrO_2/RuO_2	−62	−90	−93	−83	−90	−73	−77	−83	−94	−94	−83	−84	−63	−64
RuO_2	−73	−102	−103	−101	−99	−92	−86	−59	−69	−64	−64	−58	−46	−35
1L-RuO_2/IrO_2	−100	−125	−124	−123	−120	−110	−107	−68	−83	−81	−76	−74	−56	−54

Table S3 presents the adsorption energies of O_t and N_2 on IrO_2 and RuO_2 (110) surfaces when their lattices are exchanged to investigate strain effects. Results show minimal changes (~2 kJ mol^{-1}) in adsorption energies after lattice exchange, indicating limited strain effects. When applying IrO_2's lattice to RuO_2, adsorption energies become slightly less negative (−102 to −100 kJ mol^{-1} for O_t and −69 to −67 kJ mol^{-1} for N_2), suggesting strain effects neither significantly impact nor enhance adsorption. For IrO_2 with the RuO_2 lattice, O_t binding becomes 2 kJ mol^{-1} more negative, while N_2 binding becomes 3 kJ mol^{-1} less negative. These modest changes demonstrate that lattice exchange effects do not substantially explain the binding characteristics of these species on the (110) surfaces.

Table S3. Adsorption energies of O_t and N_2 on the (110) surfaces of IrO_2, RuO_2, calculated using original and flipped lattice parameters for each, using PBE functionals. All the values are given in kJ mol^{-1}.

O_t			N_2		
Material	Lattice		Material	Lattice	
	RuO_2	IrO_2		RuO_2	IrO_2
RuO_2	−102	−100	RuO_2	−69	−67
IrO_2	−106	−104	IrO_2	−108	−111

Figures S4 and S5 illustrate the structures and adsorption energies of O_t and N_2 species on Ir atoms in $RuO_2(110)$ mixtures and Ru atoms in $IrO_2(110)$ mixtures, respectively. The progression of the alphabetical labels corresponds to an increasing number of dopant atoms in the structure.

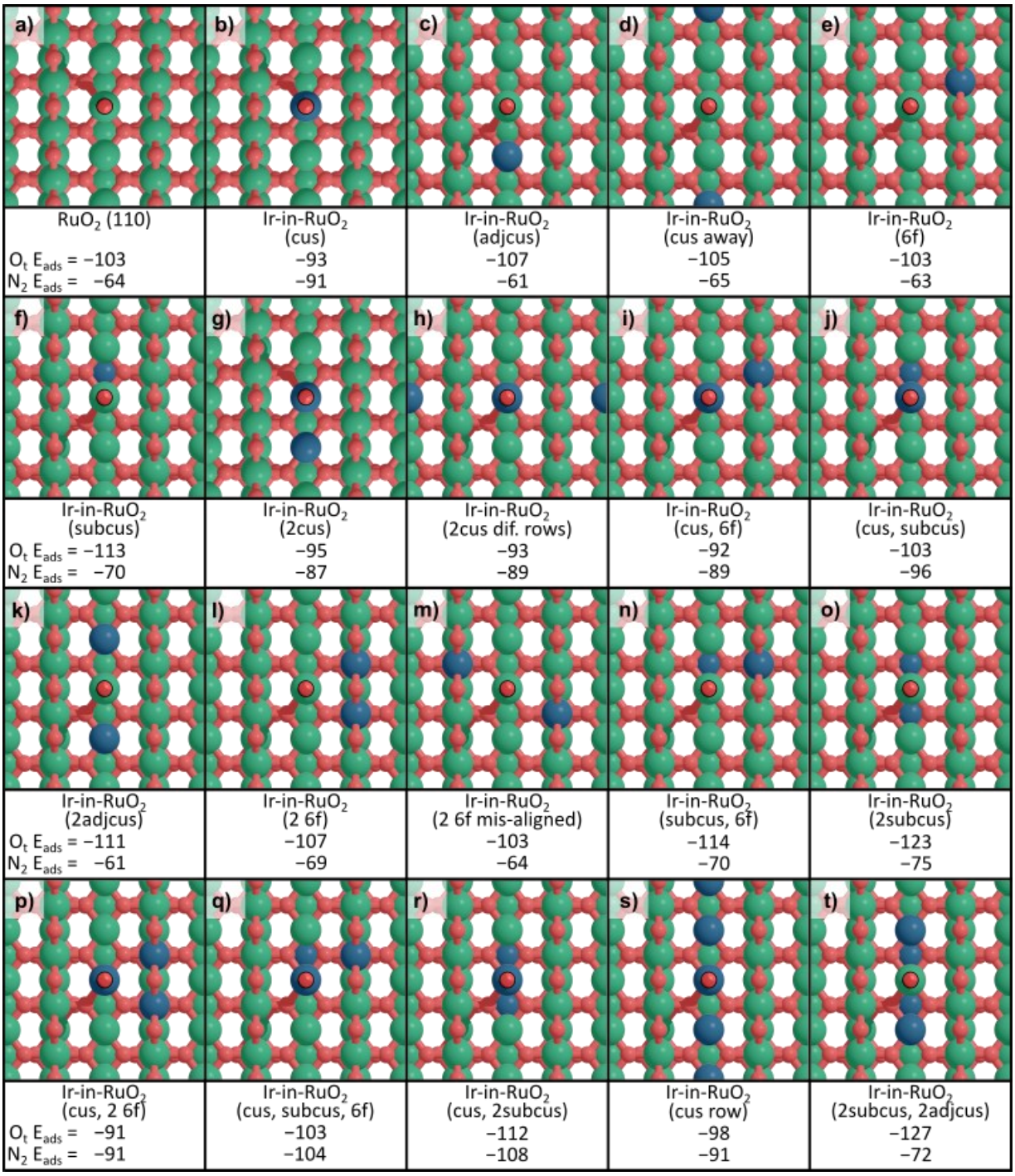

Figure S4. Structures and adsorption energies of O_t and N_2 on (a) – (ag) Ir atoms in $RuO_2(110)$ mixtures. The values are in kJ mol $^{-1}$. Green atoms represent Ru, dark blue atoms represent Ir, and red atoms represent O.

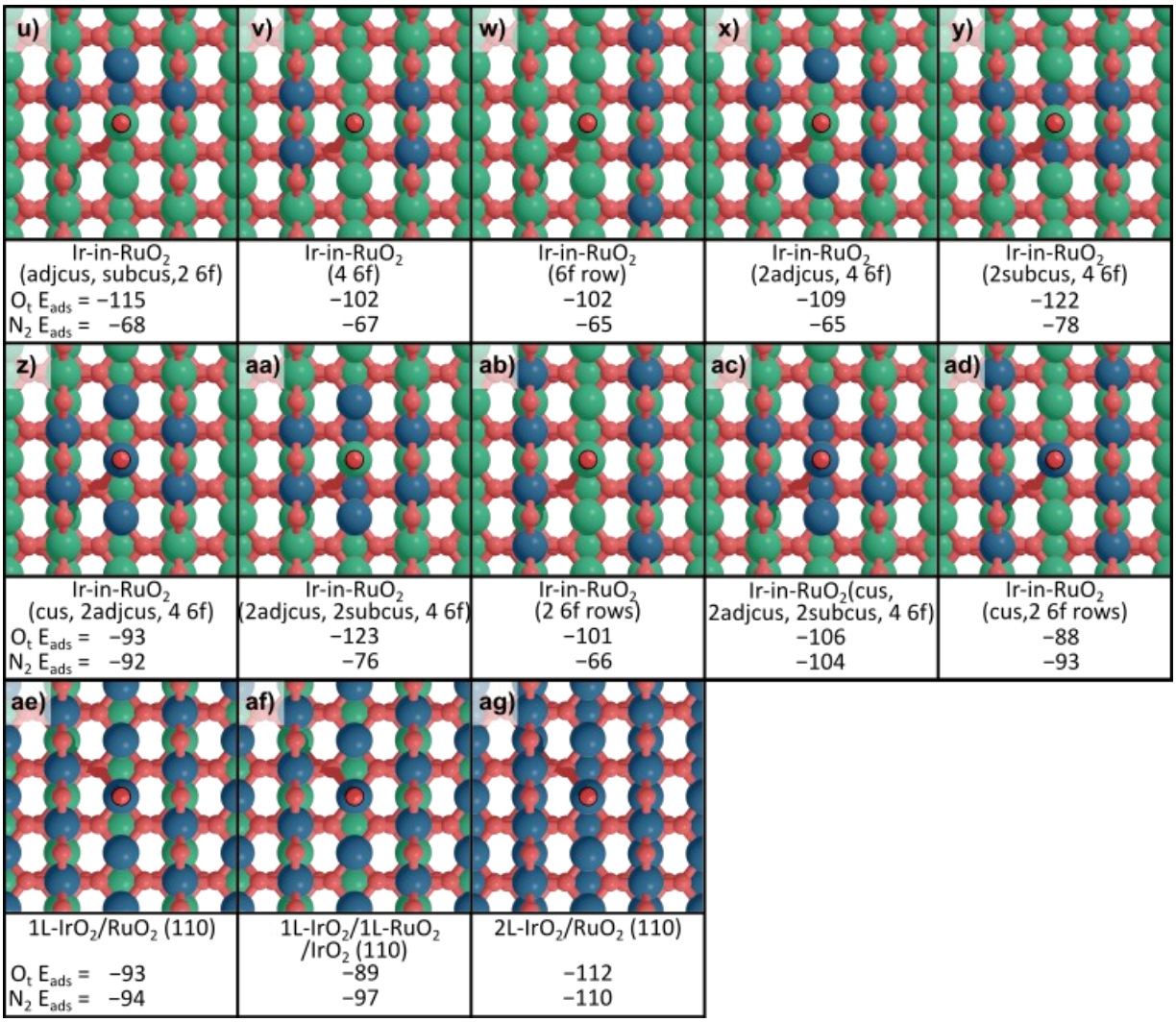

Figure S4. (continued) Structures and adsorption energies of O_t and N_2 on (a) – (ag) Ir atoms in RuO_2(110) mixtures. The values are in kJ mol $^{-1}$. Green atoms represent Ru, dark blue atoms represent Ir, and red atoms represent O.

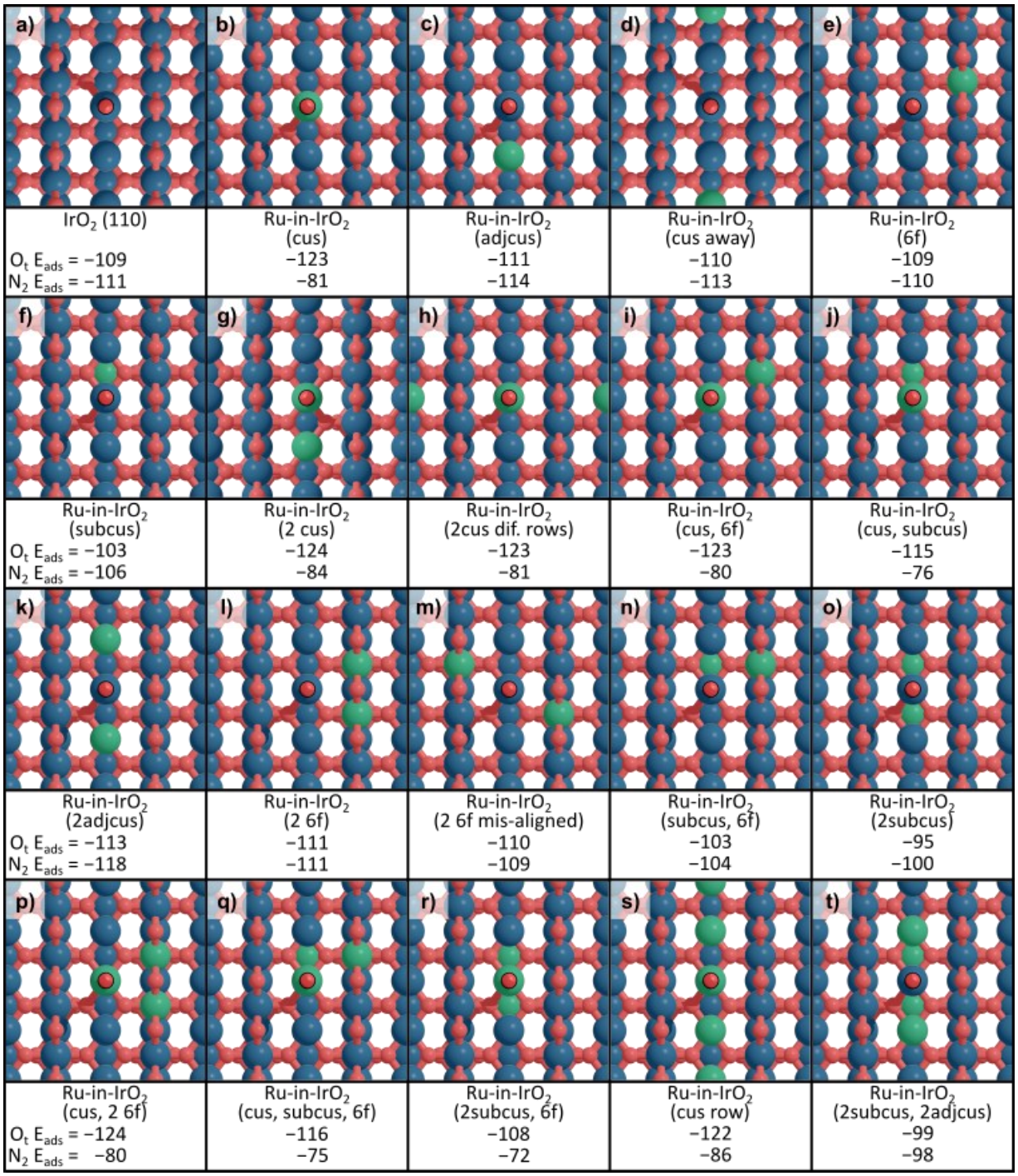

Figure S5. Structures and adsorption energies of O_t and N_2 on (a) – (ag) Ru atoms in $IrO_2(110)$ mixtures. The values are in kJ mol $^{-1}$. Green atoms represent Ru, dark blue atoms represent Ir, and red atoms represent O.

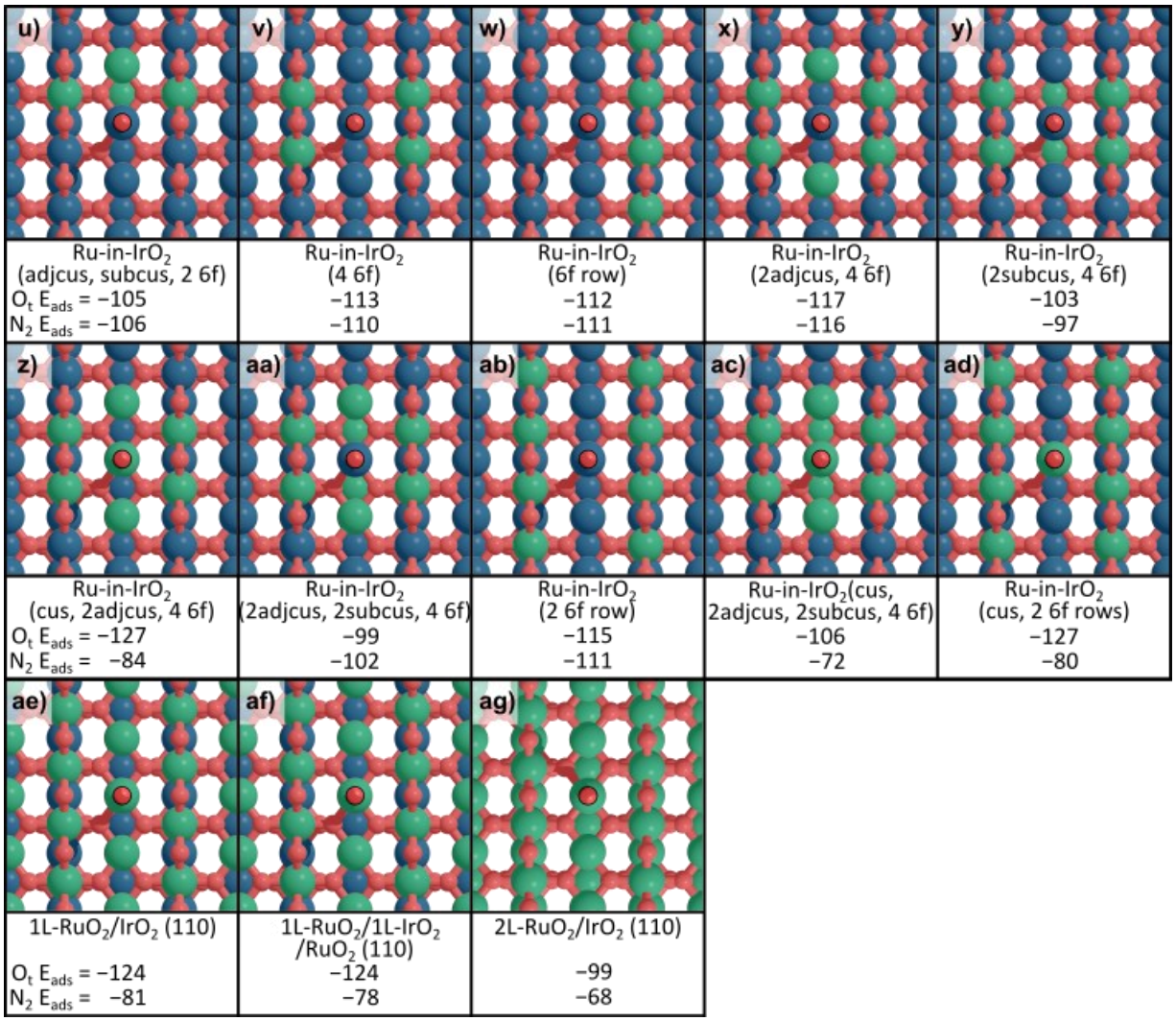

Figure S5. (continued) Structures and adsorption energies of O_t and N_2 on (a) – (ag) Ru atoms in $IrO_2(110)$ mixtures. The values are in kJ mol $^{-1}$. Green atoms represent Ru, dark blue atoms represent Ir, and red atoms represent O.

S6. Quasi-atomic orbital (QO) calculations

Occupancy matrices and atomic occupancies were computed from the plane wave DFT calculations performed in VASP using the quasi-atomic orbital (QO) method developed by Qian et al.[44] and implemented by Plaisance et al. into VASP.[45] This results in a QO basis on metal atoms consisting of the valence s and d orbitals and a QO basis on O and N consisting of the valence s and p orbitals. The occupancy matrix **P**, overlap matrix **S**, and Hamiltonian **H** in the nonorthogonal QO basis are written to output files by the QO extension to VASP following successful convergence of the electronic structure and geometry. These are then transformed to an orthonormalized QO basis according to the Löwdin procedure,

$$\mathbf{H} \rightarrow \mathbf{S}^{-\frac{1}{2}}\mathbf{H}\mathbf{S}^{-\frac{1}{2}}$$

$$\mathbf{P} \rightarrow \mathbf{S}^{\frac{1}{2}}\mathbf{P}\mathbf{S}^{\frac{1}{2}}$$

Atomic occupancies are computed from the transformed occupancy matrix,

$$q_i = \sum_{\mu \in i} P_{\mu\mu}$$

where the sum runs over all QOs on atom i.

S7. Method for decomposing charge flow during chemisorption

We have devised and implemented a method for decomposing the flow of electrons transfer between different atoms that is induced by chemisorption of a species on the surface. The method works by assigning the charge transfer to different bonding channels (σ, π_x, π_y) and then decomposing the charge transfer in each bonding channel into different electronic processes that accompany chemisorption, as indicated in Figure 9 of the main text. The decomposition proceeds in five steps:

1. Determine the pairs of entangled orbitals between the adsorbate and surface in the final (chemisorbed) state.
2. Identify the pair of entangled orbitals associated with each bonding channel.
3. Determine the relevant pairs of entangled orbitals in the bare surface (initial state).
4. Compute the atomic occupancy changes in each bonding channel associated with localization and bond formation.
5. Compute the atomic occupancy changes due to rehybridization and polarization of the surface.

Before discussing each step in detail, we will define a few quantities. The most important is the occupancy matrix **P** that defines the electronic state of the system in the quasi-atomic orbital (QO) basis. It is given by,

$$P_{\mu\nu}^{k\sigma} = \sum_n f_n^{k\sigma} \langle \phi_\mu | \psi_n^{k\sigma} \rangle \langle \psi_n^{k\sigma} | \phi_\nu \rangle$$

where the indices μ and ν run over the QOs (ϕ_μ), k and σ run over the k-points and spins, and n runs over the bands. Also, $\psi_n^{k\sigma}$ is the Bloch orbital for band n, k-point k, and spin σ, while $f_n^{k\sigma}$ is its occupancy. We use three occupancy matrices for the decomposition: the occupancy matrix computed for the final state ($\mathbf{P}_\mathrm{f}$), the occupancy matrix computed for the initial state ($\mathbf{P}_\mathrm{i}$), and the occupancy matrix computed for the initial state using the final state surface Hamiltonian ($\mathbf{P}_\mathrm{i}'$). The occupancy matrices $\mathbf{P}_\mathrm{i}$ and $\mathbf{P}_\mathrm{f}$ are computed from the output of the QO analysis performed in the VASP calculations on the initial (bare surface) and final (surface+adsorbate), respectively. This is done using an extension to VASP to perform the QO analysis that we have previously implemented. The occupancy matrix $\mathbf{P}_\mathrm{i}'$ is computed external to VASP in a Matlab code that reads in the Kohn-Sham Hamiltonian in the QO basis from the final state and extracts the submatrix corresponding to the QOs associated with the surface. It then diagonalizes this Hamiltonian for each k-point and spin to get the Bloch orbitals, calculates their occupancies using Gaussian smearing, and computes $\mathbf{P}_\mathrm{i}'$ from these orbitals and occupancies.

A complication arises from the fact that the Bloch orbitals have fractional occupancies in practical DFT calculations so that the occupancy matrix is not idempotent. While this is physically correct, it precludes analysis of entanglement between the surface and adsorbate since the occupancy matrix describes a mixed state rather than a pure state. To proceed, we use the fact that a mixed quantum state can be represented as a pure system consisting of the actual system entangled with a second system, the second system having a Hilbert space of equal dimension as the actual system.[46] Since only the dimension of the second Hilbert space is relevant, we find it convenient to simply use a copy of the Hilbert space (i.e. the QO basis) of the *actual system*, referring to this second system as the *mirror system*. This results in a 2×2 block form of the occupancy matrix $\overline{\mathbf{P}}$ in the *combined basis* of the actual and mirror systems (which together represents a pure state),

$$\overline{\mathbf{P}} = \begin{bmatrix} \mathbf{P} & \sqrt{\mathbf{P}\,(\mathbf{I}-\mathbf{P})} \\ \sqrt{\mathbf{P}\,(\mathbf{I}-\mathbf{P})} & \mathbf{I}-\mathbf{P} \end{bmatrix}$$

where $\mathbf{P}$ is the occupancy matrix of the actual system. In this form, the first block of each row or column spans the QOs of the actual system, while the second block spans the QOs of the mirror system.

Step 1 – *Determine the pairs of entangled orbitals between the adsorbate and surface in the final (chemisorbed) state*

Each bonding channel α is characterized by entanglement between a single adsorbate atomic or molecular orbital $\mathbf{a}^\alpha$ and a single surface orbital $\mathbf{b}_\mathrm{f}^\alpha$ in the final state, both represented as column vectors in the full QO basis. These pairs of orbitals can be extracted from the entanglement matrix $\mathbf{T}$ between the adsorbate and surface in the final state, obtained by left-projecting the purified occupancy matrix onto the (actual) adsorbate QOs (contained in the columns of $\mathbf{A}_0$ in the combined basis) while projecting these QOs out of it on the right,

$$\mathbf{T} = \mathbf{A}_0^\dagger \overline{\mathbf{P}}_\mathrm{f}\left(\mathbf{I} - \mathbf{A}_0\mathbf{A}_0^\dagger\right)$$

Performing a singular value decomposition on the entanglement matrix,

$$\mathbf{T} = \mathbf{Q}\mathbf{t}\mathbf{B}_\mathrm{f}^\dagger$$

allows us to compute the matrices $\mathbf{A}$ and $\mathbf{B}_\mathrm{f}$ whose columns contain pairs of the entangled orbitals $\mathbf{a}$ and $\mathbf{b}_\mathrm{f}$ between the adsorbate and surface, respectively, in the combined basis,

$$\mathbf{A} = \mathbf{A}_0\mathbf{Q}$$

The number of pairs of entangled orbitals is equal to the number of (actual) QOs on the adsorbate and is sorted in descending order based on the degree of entanglement between them, quantified by the singular values $\mathbf{t}$.

Having determined $\mathbf{A}$ and $\mathbf{B}_\mathrm{f}$, we can also determine the occupied and unoccupied combinations of the entangled orbitals in the bare surface. To do this, we first construct the matrix $\mathbf{P}_\mathrm{ab}^i$ from each pair of orbitals $\mathbf{a}^i$ and $\mathbf{b}_\mathrm{f}^i$ (the ith column vectors of $\mathbf{A}$ and $\mathbf{B}_\mathrm{f}$),

$$\mathbf{P}_\mathrm{ab}^i = \begin{bmatrix} \mathbf{a}^{i\dagger} \\ \mathbf{b}_\mathrm{f}^{i\dagger} \end{bmatrix} \overline{\mathbf{P}}_\mathrm{f}\begin{bmatrix} \mathbf{a}^i & \mathbf{b}_\mathrm{f}^i \end{bmatrix}$$

We then diagonalize each $\mathbf{P}_\mathrm{ab}^i$ to get two eigenvectors, $\mathbf{ab}^i$ (with an eigenvalue of 1) and $(\mathbf{ab}^*)^i$ (with an eigenvalue of 0). These column vectors are concatenated to form the matrices $\mathbf{AB}$ and $\mathbf{AB}^*$.

As a final step, we zero out the rows corresponding to the mirror system in the matrices $\mathbf{A}_0$, $\mathbf{A}$, $\mathbf{B}_\mathrm{f}$, $\mathbf{AB}$, and $\mathbf{AB}^*$ since these are no longer needed.

Step 2 – *Identify the pair of entangled orbitals associated with each bonding channel*

Having obtained the pairs of entangled orbitals between the adsorbate and surface, the next step is to identify which of these pairs corresponds to each of the three bonding channels α. To do this, we first we first partition the set of QOs on the adsorbate (the columns of $\mathbf{A}_0$) between the three bonding channels based on symmetry with respect to the metal-adsorbate bond axis. Since both adsorbates are axially symmetric with the bond oriented along the z-axis, we assign the O/N valence s and p_z orbitals to the σ channel and the valence p_y/p_x orbitals to the π_y/π_x channels, respectively. We then compute the quantity t^α for each of the columns $\mathbf{a}^i$ of $\mathbf{A}$, defined as,

$$t_i^\alpha = t_i \sum_{j\in\alpha} \left(\mathbf{a}^i\right)^\dagger \mathbf{a}_0^j \left(\mathbf{a}_0^j\right)^\dagger \mathbf{a}^i$$

where t_i is the degree of entanglement between the ith pair of orbitals (the singular values from Step 1), $\mathbf{a}_0^j$ is the jth column of $\mathbf{A}_0$, and the sum runs over all columns assigned to bonding channel α. Finally, we assign the single orbital pair with the highest value of t^α to bonding channel α. This is repeated for each bonding channel, so that we end up with a single orbital pair assigned to each channel. The three such adsorbate orbitals $\mathbf{a}^\alpha$ are then assigned to Set A, while the three

corresponding surface orbitals $\mathbf{b}_{\mathrm{f}}^{\alpha}$ are assigned to Set B. These column vectors are reordered in $\mathbf{A}$ and $\mathbf{B}_{\mathrm{f}}$ by the bonding channel index, while the remaining columns that were not assigned to a bonding channel are removed and added to matrices $\mathbf{A}^{\mathrm{nb}}$ and $\mathbf{B}^{\mathrm{nb}}$.

Step 3 – *Determine the relevant pairs of entangled orbitals in the bare surface (initial state)*

The three surface orbitals in Set B identified in the previous step are entangled with another set of surface orbitals (Set C) in the bare surface, prior to chemisorption. The procedure to identify these orbitals is similar to the procedure in Step 1, starting with the purified occupancy matrix of the initial state computed from $\mathbf{P}_{\mathrm{i}}'$. This is then used to compute the entanglement matrix between the orbitals in Set B and the rest of the surface. This is complicated, however, by the fact that the columns of $\mathbf{B}_{\mathrm{f}}$ are no longer orthonormal after the rows corresponding to the mirror system are zeroed out. To account for this, we first perform a singular value decomposition on B_f to get a corresponding set of orthonormal vectors in the matrix $\mathbf{B}$,

$$\mathbf{B}_{\mathrm{f}} = \mathbf{BsR}^{\dagger}$$

We compute an entanglement matrix $\mathbf{T}$ from $\overline{\mathbf{P}}_{\mathrm{i}}'$,

$$\mathbf{T} = \mathbf{B}^{\dagger}\overline{\mathbf{P}}_{\mathrm{i}}'(\mathbf{I} - \mathbf{BB}^{\dagger})$$

and perform a singular value decomposition on $\mathbf{T}$ to get matrices $\mathbf{B}_{\mathrm{i}}$ and $\mathbf{C}$ that contain pairs of entangled orbitals between Sets B and C,

$$\mathbf{T} = \mathbf{QtC}^{\dagger}$$

$$\mathbf{B}_{\mathrm{i}} = \mathbf{BQ}$$

We can also compute the occupied and unoccupied combinations of the entangled orbitals in sets B and C in the bare surface using an approach analogous to the one used in Step 1. First, we construct a matrix $\mathbf{P}_{\mathrm{bc}}^{\alpha}$ for each bonding channel from the column vectors $\mathbf{b}^{\alpha}$ and $\mathbf{c}^{\alpha}$ contained in $\mathbf{B}_{\mathrm{i}}$ and $\mathbf{C}$,

$$\mathbf{P}_{\mathrm{bc}}^{\alpha} = \begin{bmatrix} \mathbf{b}^{\alpha\dagger} \\ \mathbf{c}^{\alpha\dagger} \end{bmatrix} \overline{\mathbf{P}}_{\mathrm{f}} [\mathbf{b}^{\alpha} \quad \mathbf{c}^{\alpha}]$$

We then diagonalize this matrix for each channel to get two eigenvectors, $\mathbf{bc}^{\alpha}$ (with an eigenvalue of 1) and $(\mathbf{bc}^{*})^{\alpha}$ (with an eigenvalue of 0), which are concatenated as columns into the matrices BC and BC^{*}.

Finally, it is necessary to 'reverse' the orthonormalization that was performed at the beginning of the step by computing the matrix $\mathbf{S}$,

$$\mathbf{S} = \mathbf{Q}^{\dagger}\mathbf{sQ}$$

and using it to transform the orbitals according to,

$$\mathbf{B_i} \rightarrow \mathbf{B_i S}$$

$$\mathbf{C} \rightarrow \mathbf{C}\,\mathbf{S}$$

$$\mathbf{BC} \rightarrow \mathbf{BC}\,\mathbf{S}$$

$$\mathbf{BC}^* \rightarrow \mathbf{BC}^*\mathbf{S}$$

We finish by zeroing out the rows corresponding to the mirror system.

Step 4 – C*ompute the charge transfer in each bonding channel associated with localization and bond formation*

Having determined the orbitals in Sets A, B, and C, we now compute the change in atomic occupancies associated with localization and charge transfer. The change in the occupancy matrix due to localization in bonding channel α is given by,

$$\mathbf{\Delta P}^{\alpha}_{\mathrm{loc}} = \mathbf{c}^{\alpha} f_{\alpha} \mathbf{c}^{\alpha\dagger} + \mathbf{b}^{\alpha}_{\mathrm{i}}(1 - f_{\alpha})\mathbf{b}^{\alpha\dagger}_{\mathrm{i}} - \mathbf{b}\mathbf{c}^{\alpha}\mathbf{b}\mathbf{c}^{\alpha\dagger}$$

where f_{α} are the initial occupancies of the adsorbate orbitals in Set A associated with the bonding channels. The change in the occupancy matrix due to bond formation in channel α is computed similarly,

$$\mathbf{\Delta P}^{\alpha}_{\mathrm{bond}} = \mathbf{a}\mathbf{b}^{\alpha}\mathbf{a}\mathbf{b}^{\alpha\dagger} - \mathbf{a}^{\alpha} f_{\alpha} \mathbf{a}^{\alpha\dagger} - \mathbf{b}^{\alpha}_{\mathrm{f}}(1 - f_{\alpha})\mathbf{b}^{\alpha\dagger}_{\mathrm{f}}$$

It is also necessary to compute the change in the occupancy matrix during bond formation that is associated with entanglement of the formally nonbonding orbitals on the adsorbate with the surface. Even though these interactions are weak, they still make contributions to the atomic occupancies. To compute these, we construct matrices $\mathbf{A}^{\mathrm{nb}}$, $\mathbf{B}^{\mathrm{nb}}$, and $\mathbf{AB}^{\mathrm{nb}}$ from the columns of $\mathbf{A}$, $\mathbf{B}$, and $\mathbf{AB}$ that are not associated with any particular bonding channel,

$$\mathbf{\Delta P}^{\mathrm{nb}}_{\mathrm{bond}} = \mathbf{AB}^{\mathrm{nb}}\mathbf{AB}^{\mathrm{nb}\dagger} - \mathbf{A}^{\mathrm{nb}}\mathbf{f}^{\mathrm{nb}}\mathbf{A}^{\mathrm{nb}\dagger} - \mathbf{B}^{\mathrm{nb}}\left(\mathbf{I} - \mathbf{f}^{\mathrm{nb}}\right)\mathbf{B}^{\mathrm{nb}\dagger}$$

where $\mathbf{f}^{\mathrm{nb}}$ is a diagonal matrix with entries of 0 or 1 depending on whether the corresponding adsorbate orbital is formally unoccupied or occupied, respectively.

Once the three $\mathbf{\Delta P}$ matrices are determined, the change in occupancy on atom i can be computed as,

$$\Delta q_i = \sum_{\mu \in i} \Delta P_{\mu\mu}$$

where the sum runs over all QOs on atom i in the actual system.

Step 5 – *Compute the atomic occupancy changes due to rehybridization and polarization of the surface*

After the surface orbitals in Set B localize by disentangling with the surface orbitals in Set C, both sets of orbitals undergo additional transformations that we group together as *rehybridization*. The change in the occupancy matrix associated with this process is given by,

$$\Delta\mathbf{P}_{\mathrm{rehyb}} = \mathbf{P}_{\mathrm{f}} - \mathbf{P}_{\mathrm{i}}' - \sum_{\alpha}(\Delta\bar{\mathbf{P}}_{\mathrm{loc}}^{\alpha} + \Delta\bar{\mathbf{P}}_{\mathrm{bond}}^{\alpha}) - \Delta\bar{\mathbf{P}}_{\mathrm{bond}}^{\mathrm{nb}}$$

The only remaining contribution is due to polarization of the surface that electrostatically screens the electron redistribution occurring during the other processes. This is computed as the change in the bare surface occupancy matrix arising from the perturbation to the Kohn-Sham potential during chemisorption,

$$\Delta\mathbf{P}_{\mathrm{pol}} = \mathbf{P}_{\mathrm{i}}' - \mathbf{P}_{\mathrm{i}}$$

recalling that $\mathbf{P}_{\mathrm{i}}$ is the self-consistent occupancy matrix of the bare surface while $\mathbf{P}_{\mathrm{i}}'$ is the occupancy matrix of the bare surface computed using the Kohn-Sham potential of the chemisorbed state.

S8. Charge transfer decomposition results for the IrO_2 surface

Analogous versions of Figures 8 and 10 for the RuO_2 surface in the main text are presented in Figures S6 and S7 for the IrO_2 surface.

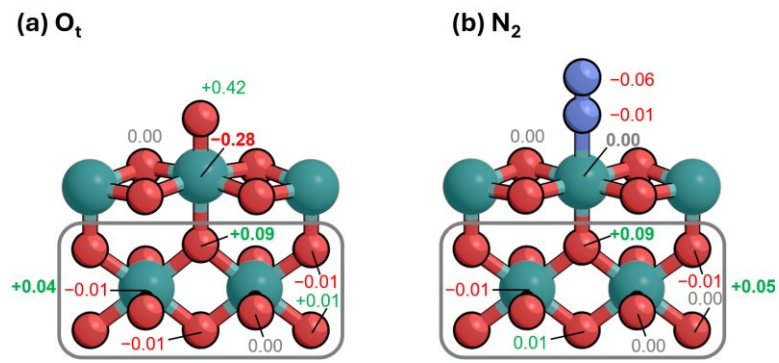

Figure S6. Changes in atomic electron occupancies induced by chemisorption of a) O_t and b) N_2 on $IrO_2(110)$. The gray box illustrates the total occupancy (0.04 for O_t and 0.05 for N_2) on the two M_{subcus} atoms and their ten O ligands. Blue-green atoms represent Ru, light blue atoms represent N, and red atoms represent O.

	bond	loc	bond+loc
σ	0.44	-0.35	0.09
π_y	-0.08	-0.36	-0.44
π_x	-0.11	-0.32	-0.43
nb	0.02		0.02
sum	0.26	-1.03	-0.77
rehyb			0.16
pol			0.33
tot			-0.29

	bond	loc	bond+loc
σ	0.26	-0.16	0.10
π_y	-0.13	0.07	-0.06
π_x	-0.11	0.04	-0.07
nb	0.00		0.00
sum	0.02	-0.05	-0.03
rehyb			-0.06
pol			0.07
tot			-0.02

(a)

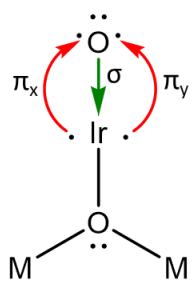

(b)

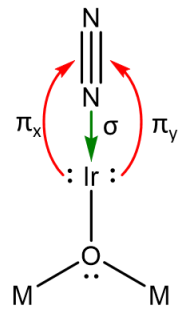

	bond	loc	bond+loc
σ	0.09	0.18	0.27
π_y	-0.04	-0.05	-0.09
π_x	-0.01	0.00	0.00
nb	0.00		0.00
sum	0.04	0.13	0.17
rehyb			-0.01
pol			-0.08
tot			0.09

	bond	loc	bond+loc
σ	0.07	0.10	0.17
π_y	-0.01	0.03	0.02
π_x	0.00	0.00	0.00
nb	0.00		0.00
sum	0.05	0.14	0.19
rehyb			0.00
pol			-0.10
tot			0.09

Figure S7. Decomposition of changes in partial atomic charges on (top) M_{cus} and (bottom) O_{sub} occurring during chemisorption of (a) O_t and (b) N_2 on IrO_2, where positive vs. negative values indicate an increase vs. decrease in electron density.

S9. Atomic occupancies of individual orbitals

The occupancy of an orbital represented as a column vector **u** (in the QO basis) on a given atom i can be computed according to,

$$q_i(\mathbf{u}) = \sum_{\mu \in i} u_\mu^* u_\mu$$

where the sum runs over all QOs on atom i. The results for the orbitals $\mathbf{b}_f$, **ab**, and $\mathbf{ab}^*$, $\mathbf{b}_i$, **c**, **bc**, and $\mathbf{bc}^*$ in each bonding channel are reported in Table S4 for O_t and Table S5 for N_2.

Table S4. Occupancies of the specified orbitals on relevant atoms for O_t adsorption on RuO_2. The occupancies are averages over all k-points and both spins.

		$\mathbf{b_f}$	**ab**	**ab***	$\mathbf{b_i}$	**c**	**bc**	**bc***
σ	M_{cus}	0.71	0.19	0.52	0.72	0.13	0.34	0.51
	O_{sub}	0.13	0.04	0.10	0.13	0.21	0.13	0.21
	O_{surf}	0.03	0.01	0.02	0.03	0.01	0.01	0.03
π_y	M_{cus}	0.53	0.15	0.38	0.53	0.05	0.51	0.07
	O_{sub}	0.11	0.03	0.08	0.11	0.01	0.05	0.07
	O_{surf}	0.03	0.01	0.02	0.03	0.00	0.01	0.02
π_x	M_{cus}	0.46	0.11	0.35	0.46	0.06	0.46	0.07
	O_{sub}	0.03	0.01	0.02	0.03	0.00	0.02	0.01
	O_{surf}	0.05	0.01	0.04	0.05	0.01	0.01	0.05

Table S5. Occupancies of the specified orbitals on relevant atoms for N_2 adsorption on RuO_2. The occupancies are averages over all k-points and both spins.

		$\mathbf{b_f}$	**ab**	**ab***	$\mathbf{b_i}$	**c**	**bc**	**bc***
σ	M_{cus}	0.74	0.11	0.63	0.74	0.15	0.21	0.68
	O_{sub}	0.18	0.03	0.15	0.18	0.23	0.20	0.21
	O_{surf}	0.01	0.00	0.01	0.01	0.02	0.02	0.01
π_y	M_{cus}	0.69	0.64	0.15	0.69	0.01	0.59	0.12
	O_{sub}	0.02	0.02	0.00	0.01	0.05	0.01	0.07
	O_{surf}	0.01	0.01	0.00	0.01	0.01	0.01	0.01
π_x	M_{cus}	0.75	0.70	0.01	0.75	0.02	0.70	0.07
	O_{sub}	0.02	0.02	0.00	0.02	0.00	0.02	0.01
	O_{surf}	0.01	0.01	0.00	0.01	0.02	0.02	0.02

S10. Comparison with charge transfer values computed using the Bader approach

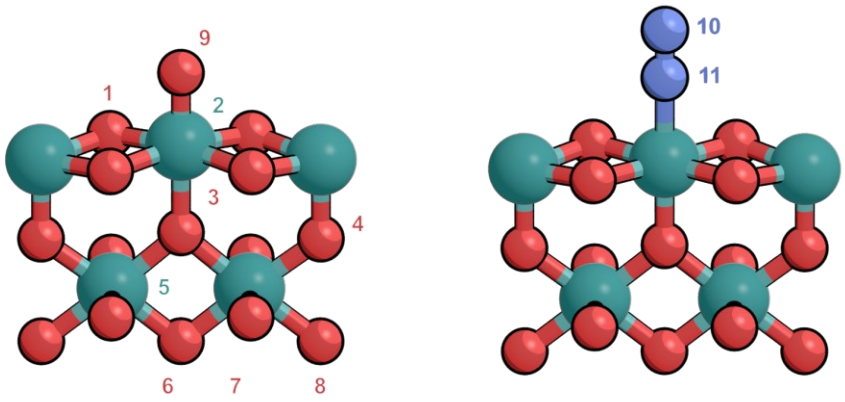

Figure S8. Labeling for atom positions in Table S6. Blue-green atoms represent Ru, light blue atoms represent N, and red atoms represent O.

Table S6. Comparison between the changes in partial atomic occupancies upon chemisorption of O and N_2 computed with the quasi-atomic orbital and Bader[47-48] approaches.

	$O@IrO_2$		$N_2@IrO_2$		$O@RuO_2$		$N_2@RuO_2$	
Atom	Bader	QO	Bader	QO	Bader	QO	Bader	QO
1	-0.02	-0.00	-0.03	0.00	-0.02	-0.00	-0.01	-0.01
2	-0.30	-0.28	-0.05	0.00	-0.26	-0.20	-0.06	0.11
3	0.04	0.09	0.07	0.09	0.09	0.13	0.03	0.09
4	-0.01	-0.01	-0.00	-0.01	-0.03	-0.02	-0.03	-0.01
5	-0.00	-0.01	0.00	-0.01	0.01	-0.01	0.02	-0.02
6	-0.00	-0.01	-0.01	-0.01	0.01	-0.01	0.01	-0.00
7	-0.00	-0.00	-0.01	-0.00	-0.01	-0.01	-0.00	-0.00
8	-0.01	0.01	-0.01	0.00	-0.01	0.01	-0.01	0.00
9	0.48	0.42	–	–	0.48	0.35	–	–
10	–	–	-0.29	-0.07	–	–	-0.28	-0.05
11	–	–	0.35	0.01	–	–	0.39	-0.01

References

1. Gerrard, A. L.; Chen, J. J.; Weaver, J. F., Oxidation of nitrided Si(100) by gaseous atomic and molecular oxygen. *J. Phys. Chem. B* **2005,** *109* (16), 8017-8028.
2. Rai, R.; Li, T.; Liang, Z.; Kim, M.; Asthagiri, A.; Weaver, J. F., Growth and termination of an IrO_2(100) film on Ir(111). *Surf. Sci.* **2016,** *652*, 213-221.
3. Kan, H. H.; Shumbera, R. B.; Weaver, J. F., Adsorption and abstraction of oxygen atoms on Pd(111): Characterization of the precursor to PdO formation. *Surf. Sci.* **2008,** *602* (7), 1337-1346.
4. Cartas, W.; Rai, R.; Sathe, A.; Schaefer, A.; Weaver, J. F., Oxidation of a Tb_2O_3(111) thin film on Pt(111) by gas-phase oxygen atoms. *J. Phys. Chem. C* **2014,** *118* (36), 20916-20926.
5. Jamir, J.; Yun, J.; Pope, C.; Kim, M.; Asthagiri, A.; Weaver, J. F., Ethane adsorption and oxidation on IrO_2(110) surfaces. *J. Phys. Chem. C* **2024,** *128* (1), 111-122.
6. Li, T.; Kim, M.; Liang, Z.; Asthagiri, A.; Weaver, J., Hydrogen oxidation on oxygen-rich IrO_2(110). *Catal., Struct. React.* **2018,** *4*, 1-13.
7. Kim, M.; Franklin, A.; Martin, R.; Feng, F.; Li, T.; Liang, Z.; Asthagiri, A.; Weaver, J., Adsorption and oxidation of CH_4 on oxygen-rich IrO_2(110). *J. Phys. Chem. C* **2019,** *123* (45), 27603-27614.
8. Lee, C. J.; Vashishtha, S.; Shariff, M.; Zou, F. R.; Shi, J. J.; Meyer, R. J.; Weaver, J. F., Kinetics and selectivity of methane oxidation on an IrO_2(110) film. *J. Phys.: Condens. Matter* **2022,** *34* (28), 284002.
9. Martin, R.; Kim, M.; Lee, C. J.; Shariff, M. S.; Feng, F.; Meyer, R. J.; Asthagiri, A.; Weaver, J. F., Molecular chemisorption of N_2 on IrO_2(110). *J. Chem. Phys.* **2020,** *152* (7), 074712.
10. Abb, M. J. S.; Herd, B.; Over, H., Template-assisted growth of ultrathin single-crystalline IrO_2(110) films on RuO_2(110)/Ru(0001) and its thermal stability. *J. Phys. Chem. C* **2018,** *122* (26), 14725-14732.
11. Abb, M. J. S.; Weber, T.; Langsdorf, D.; Koller, V.; Gericke, S. M.; Pfaff, S.; Busch, M.; Zetterberg, J.; Preobrajenski, A.; Gronbeck, H.; Lundgren, E.; Over, H., Thermal stability of single-crystalline IrO_2(110) layers: Spectroscopic and adsorption studies. *J. Phys. Chem. C* **2020,** *124*, 15324-15336.
12. Sen, F. G.; Kinaci, A.; Narayanan, B.; Gray, S. K.; Davis, M. J.; Sankaranarayanan, S. K. R. S.; Chan, M. K. Y., Towards accurate prediction of catalytic activity in IrO_2 nanoclusters via first principles-based variable charge force field. *J. Mater. Chem. A* **2015,** *3* (37), 18970-18982.
13. Pope, C.; Yun, J.; Reddy, R.; Jamir, J.; Kim, D.; Kim, M.; Asthagiri, A.; Weaver, J. F., Surface chlorination of IrO_2(110) by HCl. *J. Chem. Phys.* **2024,** *161* (6), 064704.
14. Rai, R.; Weaver, J. F., Methanol oxidation on stoichiometric and oxygen-rich RuO_2(110). *Phys. Chem. Chem. Phys.* **2017,** *19* (29), 18975-18987.
15. Liang, Z.; Kim, M.; Li, T.; Rai, R.; Asthagiri, A.; Weaver, J. F., Adsorption and oxidation of ethylene on the stoichiometric and O-rich RuO_2(110) surfaces. *J. Phys. Chem. C* **2017,** *121* (37), 20375-20386.
16. Li, T.; Rai, R.; Liang, Z.; Kim, M.; Asthagiri, A.; Weaver, J. F., Adsorption and oxidation of n-butane on the stoichiometric RuO_2(110) surface. *J. Phys. Chem. C* **2016,** *120* (18), 9863-9873.
17. Li, T.; Kim, M.; Rai, R.; Liang, Z.; Asthagiri, A.; Weaver, J. F., Adsorption of alkanes on stoichiometric and oxygen-rich RuO_2(110). *Phys. Chem. Chem. Phys.* **2016,** *18* (32), 22647-22660.
18. Over, H., Surface chemistry of ruthenium dioxide in heterogeneous catalysis and electrocatalysis: From fundamental to applied research. *Chem. Rev.* **2012,** *112* (6), 3356-3426.
19. Powell, C. J.; Jablonski, A., NIST Electron Inelastic-Mean-Free-Path Database. In *National Institute of Standards and Technology*, Gaithersburg, Maryland 20899, 2010.
20. Hochella, M. F.; Carim, A. H., A Reassessment of Electron-Escape Depths in Silicon and Thermally Grown Silicon Dioxide Thin-Films. *Surf. Sci.* **1988,** *197* (3), L260-L268.
21. Redhead, P. A., Thermal desorption of gases. *Vacuum* **1962,** *12* (4), 203-211.
22. Antony, A.; Asthagiri, A.; Weaver, J. F., Pathways and kinetics of methane and ethane C-H bond cleavage on PdO(101). *J. Chem. Phys.* **2013,** *139*, 104702: 1-12.
23. Martin, R.; Kim, M.; Franklin, A.; Bian, Y.; Asthagiri, A.; Weaver, J. F., Adsorption and oxidation of propane and cyclopropane on IrO_2(110). *Phys. Chem. Chem. Phys.* **2018,** *20*, 29264 - 29273.
24. Li, T.; Kim, M.; Liang, Z.; Asthagiri, A.; Weaver, J. F., Dissociative chemisorption and oxidation of H_2 on the stoichiometric IrO_2(110) surface. *Top. Catal.* **2018,** *61* (5-6), 397-411.
25. Liang, Z.; Li, T.; Kim, M.; Asthagiri, A.; Weaver, J. F., Low-temperature activation of methane on the IrO_2(110) surface. *Science* **2017,** *356* (6335), 299-303.
26. Weaver, J. F., Surface chemistry of late transition metal oxides. *Chem. Rev.* **2013,** *113*, 4164−4215.
27. Kresse, G.; Hafner, J., Abinitio Molecular-Dynamics for Liquid-Metals. *Phys. Rev. B* **1993,** *47* (1), 558-561.

28. Kresse, G.; Hafner, J., Ab-initio molecular-dynamics simulation of the liquid-metal amorphous-semiconductor transition in germanium. *Phys. Rev. B* **1994,** *49* (20), 14251-14269.
29. Kresse, G.; Furthmuller, J., Efficient iterative schemes for ab initio total-energy calculations using a plane-wave basis set. *Phys. Rev. B* **1996,** *54* (16), 11169-11186.
30. Kresse, G.; Furthmuller, J., Efficiency of ab-initio total energy calculations for metals and semiconductors using a plane-wave basis set. *Comp. Mater. Sci.* **1996,** *6* (1), 15-50.
31. Kravchenko, P.; Plaisance, C.; Hibbitts, D., A new computational interface for catalysis. **2019**.
32. Perdew, J. P.; Burke, K.; Ernzerhof, M., Generalized gradient approximation made simple. *Phys. Rev. Lett.* **1996,** *77* (18), 3865.
33. Hammer, B.; Hansen, L. B.; Norskov, J. K., Improved adsorption energetics within density-functional theory using revised Perdew-Burke-Ernzerhof functionals. *Phys. Rev. B* **1999,** *59* (11), 7413-7421.
34. Wellendorff, J.; Lundgaard, K. T.; Mogelhoj, A.; Petzold, V.; Landis, D. D.; Norskov, J. K.; Bligaard, T.; Jacobsen, K. W., Density functionals for surface science: Exchange-correlation model development with Bayesian error estimation. *Phys. Rev. B* **2012,** *85* (23).
35. Blochl, P. E., Projector augmented-wave method. *Phys. Rev. B* **1994,** *50* (24), 17953-17979.
36. Kresse, G.; Joubert, D., From ultrasoft pseudopotentials to the projector augmented-wave method. *Phys. Rev. B* **1999,** *59* (3), 1758-1775.
37. Grimme, S.; Antony, J.; Ehrlich, S.; Krieg, H., A consistent and accurate ab initio parametrization of density functional dispersion correction (DFT-D) for the 94 elements H-Pu. *J. Chem. Phys.* **2010,** *132* (15), 154104.
38. Grimme, S.; Ehrlich, S.; Goerigk, L., Effect of the Damping Function in Dispersion Corrected Density Functional Theory. *J. Comput. Chem.* **2011,** *32* (7), 1456-1465.
39. Pan, L.; Weaver, J. F.; Asthagiri, A., First Principles Study of Molecular O_2 Adsorption on the PdO(101) Surface. *Top. Catal.* **2017,** *60* (6-7), 401-412.
40. Wang, H. Y.; Schneider, W. F., Effects of coverage on the structures, energetics, and electronics of oxygen adsorption on RuO_2(110). *J. Chem. Phys.* **2007,** *127* (6), 064706.
41. Jónsson, H.; Mills, G.; Jacobsen, K. W., Nudged Elastic Band Method for Finding Minimum Energy Paths of Transitions. In *In Classical and Quantum Dynamics in Condensed Phase Simulations*, Berne, B. J., Ciccotti, G., Coker, D. F., Ed. World Scientific: 1998; pp 385–404.
42. Henkelman, G.; Jonsson, H., Improved tangent estimate in the nudged elastic band method for finding minimum energy paths and saddle points. *J. Chem. Phys.* **2000,** *113* (22), 9978-9985.
43. Henkelman, G.; Jonsson, H., A dimer method for finding saddle points on high dimensional potential surfaces using only first derivatives. *J. Chem. Phys.* **1999,** *111* (15), 7010-7022.
44. Qian, X. F.; Li, J.; Qi, L.; Wang, C. Z.; Chan, T. L.; Yao, Y. X.; Ho, K. M.; Yip, S., Quasiatomic orbitals for ab initio tight-binding analysis. *Phys. Rev. B* **2008,** *78* (24), 245112.
45. Plaisance, C. P.; van Santen, R. A.; Reuter, K., Constrained-Orbital Density Functional Theory. Computational Method and Applications to Surface Chemical Processes. *J. Chem. Theory Comput.* **2017,** *13* (8), 3561-3574.
46. Knizia, G.; Chan, G. K. L., Density Matrix Embedding: A Simple Alternative to Dynamical Mean-Field Theory. *Phys. Rev. Lett.* **2012,** *109* (18), 186404.
47. Tang, W.; Sanville, E.; Henkelman, G., A grid-based Bader analysis algorithm without lattice bias. *J. Phys.: Condens. Matter* **2009,** *21* (8), 084204.
48. Yu, M.; Trinkle, D. R., Accurate and efficient algorithm for Bader charge integration. *J. Chem. Phys.* **2011,** *134* (6), 064111.